



HAL
open science

Evidence of depolarization and ellipticity of high harmonics driven by ultrashort bichromatic circularly polarized fields

Lou Barreau, Kévin Veyrinas, Vincent Gruson, Sébastien J. Weber, Thierry Auguste, Jean-François Hergott, Fabien Lepetit, Bertrand Carre, Jean-Christophe Houver, Danielle Doweck, et al.

► To cite this version:

Lou Barreau, Kévin Veyrinas, Vincent Gruson, Sébastien J. Weber, Thierry Auguste, et al.. Evidence of depolarization and ellipticity of high harmonics driven by ultrashort bichromatic circularly polarized fields. *Nature Communications*, 2018, 9, pp.4727. 10.1038/s41467-018-07151-8 . cea-01934789

HAL Id: cea-01934789

<https://cea.hal.science/cea-01934789>

Submitted on 28 Feb 2019

HAL is a multi-disciplinary open access archive for the deposit and dissemination of scientific research documents, whether they are published or not. The documents may come from teaching and research institutions in France or abroad, or from public or private research centers.

L'archive ouverte pluridisciplinaire **HAL**, est destinée au dépôt et à la diffusion de documents scientifiques de niveau recherche, publiés ou non, émanant des établissements d'enseignement et de recherche français ou étrangers, des laboratoires publics ou privés.

ARTICLE

DOI: 10.1038/s41467-018-07151-8

OPEN

Evidence of depolarization and ellipticity of high harmonics driven by ultrashort bichromatic circularly polarized fields

Lou Barreau¹, Kévin Veyrinas², Vincent Gruson ¹, Sébastien J. Weber^{1,3}, Thierry Auguste¹, Jean-François Hergott¹, Fabien Lepetit¹, Bertrand Carré¹, Jean-Christophe Houver², Danielle Doweck² & Pascal Salières ¹

High harmonics generated by counter-rotating laser fields at the fundamental and second harmonic frequencies have raised important interest as a table-top source of circularly polarized ultrashort extreme-ultraviolet light. However, this emission has not yet been fully characterized: in particular it was assumed to be fully polarized, leading to an uncertainty on the effective harmonic ellipticity. Here we show, through simulations, that ultrashort driving fields and ultrafast medium ionization lead to a breaking of the dynamical symmetry of the interaction, and consequently to deviations from perfectly circular and fully polarized harmonics, already at the single-atom level. We perform the complete experimental characterization of the polarization state of high harmonics generated along that scheme, giving direct access to the ellipticity absolute value and sign, as well as the degree of polarization of individual harmonic orders. This study allows defining optimal generation conditions of fully circularly polarized harmonics for advanced studies of ultrafast dichroisms.

¹LIDYL, CEA, CNRS, Université Paris-Saclay, CEA Saclay, 91191 Gif-sur-Yvette, France. ²Institut des Sciences Moléculaires d'Orsay (ISMO), CNRS, Univ. Paris-Sud, Université Paris-Saclay, F-91405 Orsay, France. ³CEMES, UPR 8011, CNRS-Université de Toulouse, 29, rue Jeanne Marvig, BP 94347, F-31055 Toulouse, France. These authors contributed equally: Lou Barreau, Kévin Veyrinas, Vincent Gruson. Correspondence and requests for materials should be addressed to D.D. (email: danielle.doweck@u-psud.fr) or to P.S. (email: pascal.salieres@cea.fr)

Circularly-polarized light is a remarkable probe of chirality¹ and magnetization^{2,3}. The advent of ultrashort pulses in the extreme ultraviolet (XUV) and soft X-ray ranges of perfectly known and controllable polarization hold the promise of studying these phenomena on the (sub-)femtosecond natural timescales of electronic dynamics and magnetic interactions^{4,5}, with atomic selectivity^{6,7}. Remarkable progress has been achieved recently to provide tunable polarization of X-ray free-electron lasers, and to characterize the polarization state by combining different techniques^{8,9}. Ultrashort table-top high-harmonic generation (HHG) sources have long been confined to low ellipticities^{10–15} until recently when various schemes were shown to produce a high degree of circularity^{4,16–21}. A particular scheme proposed long ago^{22,23} stands out as a good candidate to produce intense circularly-polarized ultrashort XUV pulses and has triggered a lot of theoretical^{24–30} and experimental work^{17,18,31,32}. In this scheme, the HHG is driven by two counter-rotating circularly polarized pulses at the fundamental and second harmonic frequencies. In the idealized case of perfectly periodic driving fields and isotropic time-independent medium, the threefold dynamical symmetry imposes the emission of all the odd and even harmonics except the $3q$, with the $3q+1$ ($3q+2$) harmonics circularly polarized with the same helicity as the ω (2ω) driver, respectively^{17,18,24,33}.

Nevertheless, the complete measurement of the harmonic polarization state (that is, the simultaneous measurement of all three Stokes parameters³⁴ for each order) has not yet been performed, to the best of our knowledge. On the one hand, the degree of linear polarization (related to the normalized Stokes parameters s_1 and s_2) were measured using optical polarimetry¹⁷. On the other hand, the degree of circular polarization (related to the normalized Stokes parameter s_3) was independently measured, in different generation conditions, using X-ray magnetic circular dichroism^{18,32}. In all studies, the harmonic emission was considered fully polarized ($\sqrt{s_1^2 + s_2^2 + s_3^2} = 1$), which allows calculating an apparent ellipticity. If this were not the case, that is, if some depolarization were present, the true ellipticity of the polarized part of the radiation would be different. Actually, very few articles have discussed possible causes of depolarization in HHG so far, only in the single color case, and with elliptical driver¹³ or generation in clusters³⁵.

The recent theoretical and experimental effort has concentrated on the control of the intensity ratio between the $3q+1$ and the $3q+2$ orders³⁰, using phase matching^{18,36}, the electronic structure of the generation medium^{28,31,37,38}, the intensity of the driving fields³⁹, or, in a very early study, a strong magnetic field⁴⁰. This ratio is important for determining the polarization of the attosecond pulse train (APT) composed of all harmonic orders. Obviously, the exact polarization of each order is another key element that needs to be determined.

Here we numerically and experimentally show that high harmonics generated by ultrashort counter-rotating ω and 2ω fields are in general neither purely circular nor fully polarized. In contrast to the usual picture of momentum conservation laws^{17,26,27}, time-dependent Schrödinger equation (TDSE) calculations show that elliptical harmonics can already appear at the single-atom level, even in the case of perfectly circular driving fields and isotropic generating medium, resulting from short-pulse envelope effects or fast ionization. Significant deviations from circularity and depolarization are furthermore evidenced by a complete experimental characterization of the polarization state of high harmonics generated in argon, performed with the molecular polarimetry method^{41,42}. The molecular frame photoelectron angular distributions (MFPAD) characterizing photoionization of NO molecules provide simultaneously all three Stokes parameters of the XUV light—including

the challenging disentanglement of the circular and unpolarized components.

Results

Breaking of the dynamical symmetry. The combined electric field of the counter-rotating ω and 2ω beams has a threefold rosette shape (Fig. 1b). The electron wavepackets released through tunnel ionization of the target gas close to each field maximum are accelerated and finally recollide with the parent ion every $1/3$ of ω cycle²⁴. In an isotropic and time-independent medium, this leads to the emission of attosecond pulses of equal intensity every $T/3$, linearly polarized (along the recollision direction) with an orientation increasing by 120° every $T/3$ ⁴³. This threefold dynamical symmetry imposes emission of only the $3q+1$ and $3q+2$ harmonic orders with circular polarization and helicity of the ω and 2ω fields, respectively^{18,24,33}. Any breaking of symmetry between the three atto-pulses in the ω cycle would result in a decreased harmonic ellipticity, emission of the $3q$ harmonic orders and possibly depolarization. Such breaking can be induced either by the driving fields (elliptical polarization^{24,32} or imperfect overlap⁴⁴) or by the anisotropic generating medium^{31,45}. By solving the TDSE, we show that such breaking can occur even for perfectly circular driving fields and in an isotropic medium, when the strong-field interaction leading to the harmonic emission presents sub- ω cycle modulations due to (i) a fast temporal variation of the driving laser fields on the envelope rising and falling edges, causing temporal variations of the harmonic dipole vector; (ii) ionization of the medium resulting in a fast decay of the induced dipole strength with time.

The above sources of temporal asymmetry result in a spectral broadening of each harmonic peak with spectrally-varying polarization properties. Ultrafast dichroism measurements involve the polarization characteristics of the short harmonic temporal pulses, that is, the ones calculated over the spectrally-integrated harmonic peaks. The temporal/spectral variations of the polarization may result in a significant amount of depolarization.

A first temporal asymmetry, introduced by the fast variation of the driving fields on the pulse edges, results in a modification of the quantum trajectories leading to the harmonic emission. The recollision time, direction and probability that respectively influence the phase, polarization and intensity of the attosecond emission deviate rapidly (within a ω cycle) from the constant-envelope case (by dt , da , and dI , respectively in Fig. 1b). These variations decrease the ellipticity and polarization degree of the harmonic peaks, as evidenced by TDSE calculations in helium at intensities low enough to avoid significant (<2%) depletion of the medium due to ionization (Fig. 1). The harmonic spectra (Fig. 1d) show well-defined peaks at low orders due to the short electron trajectories (travel time shorter than $0.5T$) giving the dominant contributions to the harmonic emission²⁴. However, the peaks broaden considerably with increasing order leading to an overlap of neighboring orders above H32 and a mixing of their polarization properties. This broadening is a direct consequence of the inter-cycle temporal modulation of the harmonic dipole phase in the laser envelope^{46–49}. The resulting harmonic chirp^{50–54} leads to a blue-shift of the central frequency on the rising edge and a red-shift on the falling edge, as evidenced by a Gabor time-frequency analysis of the harmonic intensity (Fig. 1c) and ellipticity (Fig. 1e). For the plateau harmonics (H19–31), the Gabor spectrograms reveal a roughly constant central frequency but an ellipticity almost opposite on the pulse edges as compared to the central part, due to the fast intra-cycle variations illustrated in Fig. 1b. Consequently, the harmonic ellipticity corresponding to the emission during the

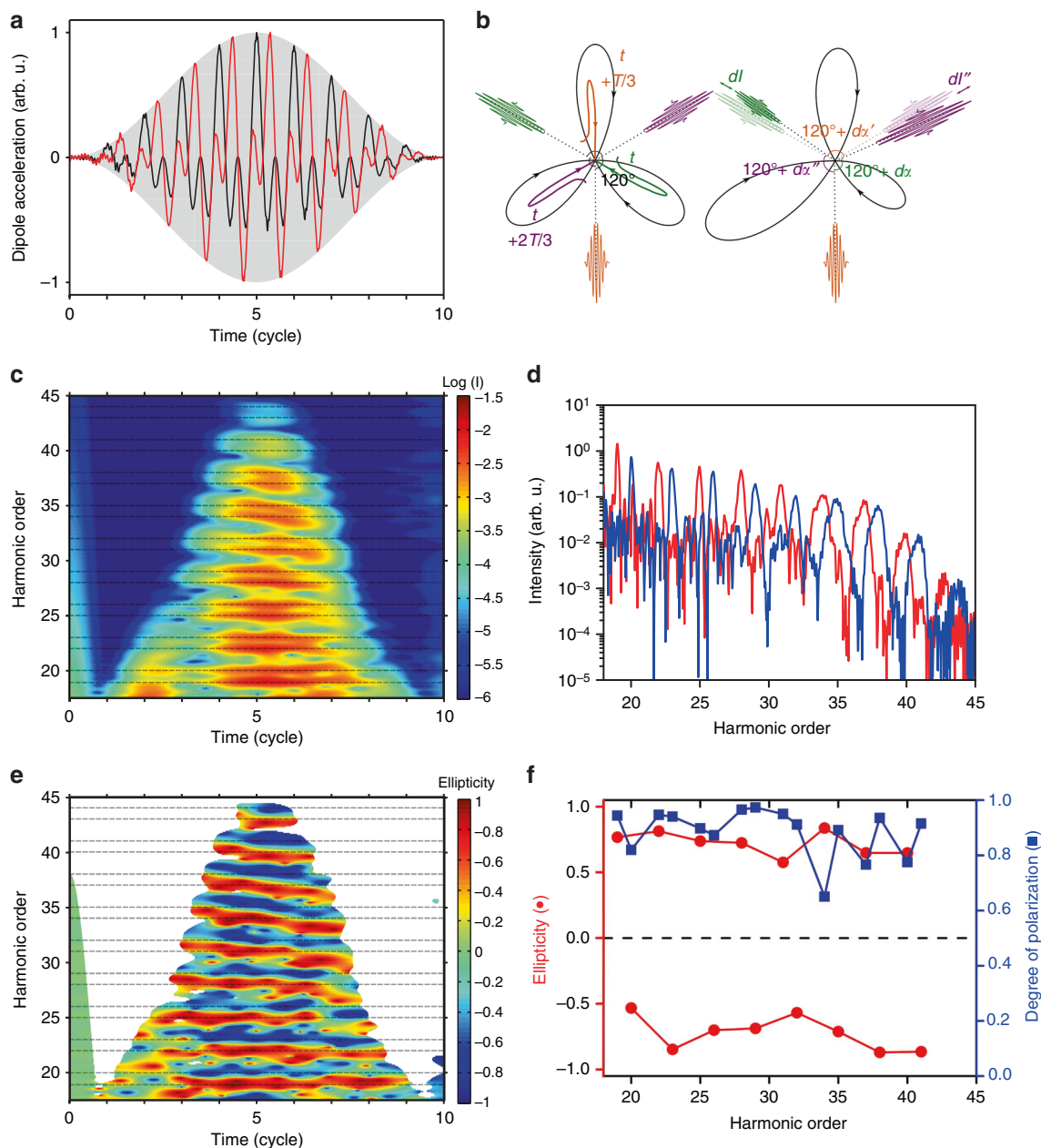


Fig. 1 Short-pulse envelope effects in helium. **a** Dipole acceleration along the x and y components resulting from the interaction of a helium atom with 800- and 400-nm pulses (\sin^2 envelope with 5 ω -cycle full-width-at-half-maximum (FWHM) duration, shaded gray) at $I_\omega = I_{2\omega} = 2 \times 10^{14}$ W/cm². **b** Illustration of the harmonic generation process for a constant laser envelope (left) and on a short-pulse leading edge (right). Typical electron trajectories²⁴ launched every $T/3$ of the total driving field (black) are shown in lines of different colors together with the corresponding attosecond pulses emitted at recollision. **c** Time-frequency representation of the harmonic intensity, in logarithmic scale, obtained after Gabor transformation of the dipole shown in **(a)** with a temporal Gaussian window of one- ω -cycle FWHM. **d** Corresponding harmonic spectra for the components co-rotating (red) or counter-rotating (blue) with the ω field. **e** Time-frequency representation of the harmonic ellipticity, showing the alternating helicity of the $3q+1$ and $3q+2$ harmonics. **f** Ellipticity and degree of polarization calculated over the harmonic spectral width (± 0.25 order until H32 and ± 0.5 order for higher energies)

whole pulse is significantly reduced for all orders to 0.5–0.8, and the depolarization reaches 5 to 10%, and up to 20% for high orders (Fig. 1f). Note that these short-pulse envelope effects depend on the carrier-envelope phase (CEP) and are still significant for 10-cycle FWHM driving fields (Supplementary Note 4).

A second temporal asymmetry arises from the medium ionization that leads to a decay of the emission efficiency inside the driving envelope. In the bicircular counter-rotating case, the generation medium ionizes much faster than with a linearly polarized field²⁴, as illustrated in Fig. 2a for argon. In order to

separate this effect from the short-pulse envelope effects discussed above, the simulations are now performed for trapezoidal envelopes (two-cycle turn-on and turn-off and six cycles of constant amplitude), ensuring a constant maximum field strength in the central part of the pulse. There, the dynamical symmetry breaking can only occur in the target, namely through a fast atomic ionization depleting the generating medium. The spectrograms in Fig. 2b, c show two different regions. During the first two cycles, the harmonics are strongly blue-shifted, and their polarization is far from circular. These short-pulse envelope effects are similar to the ones discussed above. During the

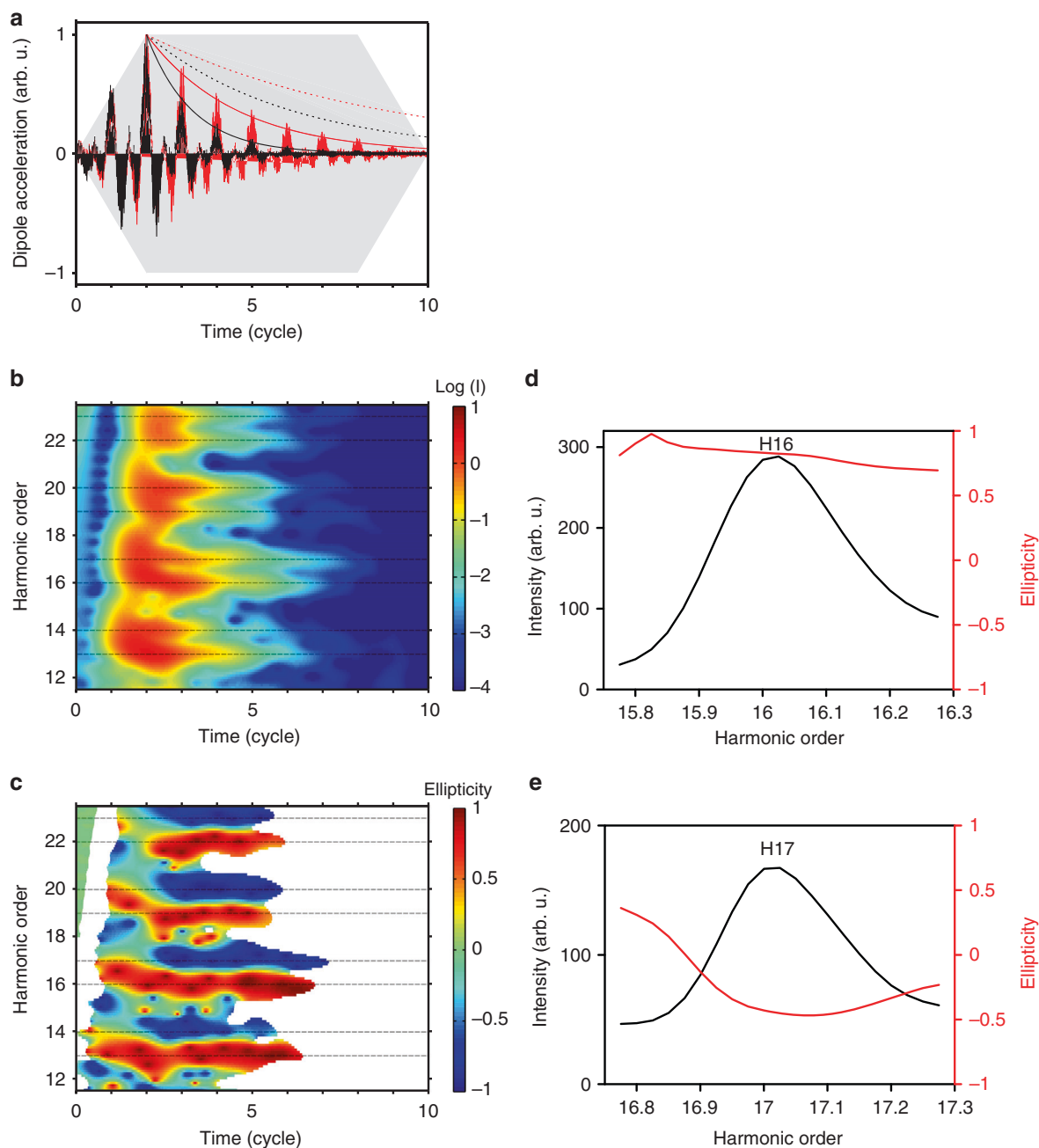


Fig. 2 Ionization effects in argon. **a** Dipole acceleration along the x axis calculated for trapezoidal pulses (shaded gray area) in argon at intensities $I_0 = I_\omega = I_{2\omega} = 8 \times 10^{13}$ (red) and 1.2×10^{14} W/cm² (black) and their envelopes (exponential solid lines). At 1.2×10^{14} W/cm², only the first cycles contribute to the emission due to strong ionization. We show for comparison the dipole envelopes calculated with a linearly-polarized IR pulse of same total energy $I_\omega = 2I_0 = 1.6 \times 10^{14}$ (red dashed line) and 2.4×10^{14} W/cm² (black dotted line). **b** Time-frequency representation of the harmonic intensity, in logarithmic scale, for $I_0 = 1.2 \times 10^{14}$ W/cm², obtained after Gabor transformation of the dipole with a temporal Gaussian window of one- ω -cycle FWHM. **c** Time-frequency representation of the harmonic ellipticity for $I_0 = 1.2 \times 10^{14}$ W/cm². **d, e** Spectrum (black) and spectrally-resolved ellipticity (red) of harmonics 16 and 17 for $I_0 = 1.2 \times 10^{14}$ W/cm²

following cycles, where the envelope is constant, the central frequency and polarization properties are extremely stable with time. However, the circularity is not perfect ($|\epsilon| \approx 0.85$) due to the exponentially decreasing harmonic efficiency with time, as recovered by a simple model (see Supplementary Note 6). In the corresponding harmonic spectra (Fig. 2d, e), the $3q+1$ orders exhibit quite constant polarization properties over the harmonic width, in contrast to the $3q+2$ orders that present much lower and fastly-varying ellipticity, in particular on the low-energy side. This is due to the strong blue-shift of orders $3q+1$ on the rising

edge leading to an overlap with the $3q+2$. When the ellipticities are calculated over the integrated harmonic peaks, their values deviate significantly from ± 1 ($|\epsilon| \approx 0.8$ for $3q+1$ and $|\epsilon| \approx 0.5$ for $3q+2$) and depolarization appears, mainly for $3q+2$ orders (10–20%) (Fig. 3e, f).

We now revisit the influence of an additional breaking of symmetry brought about by a slight deviation from circularity of the ω field, the 2ω field remaining circular. When the ω field ellipticity decreases, the $3q$ harmonic intensity increases (Fig. 3a–c), and the harmonic ellipticity quickly drops in modulus

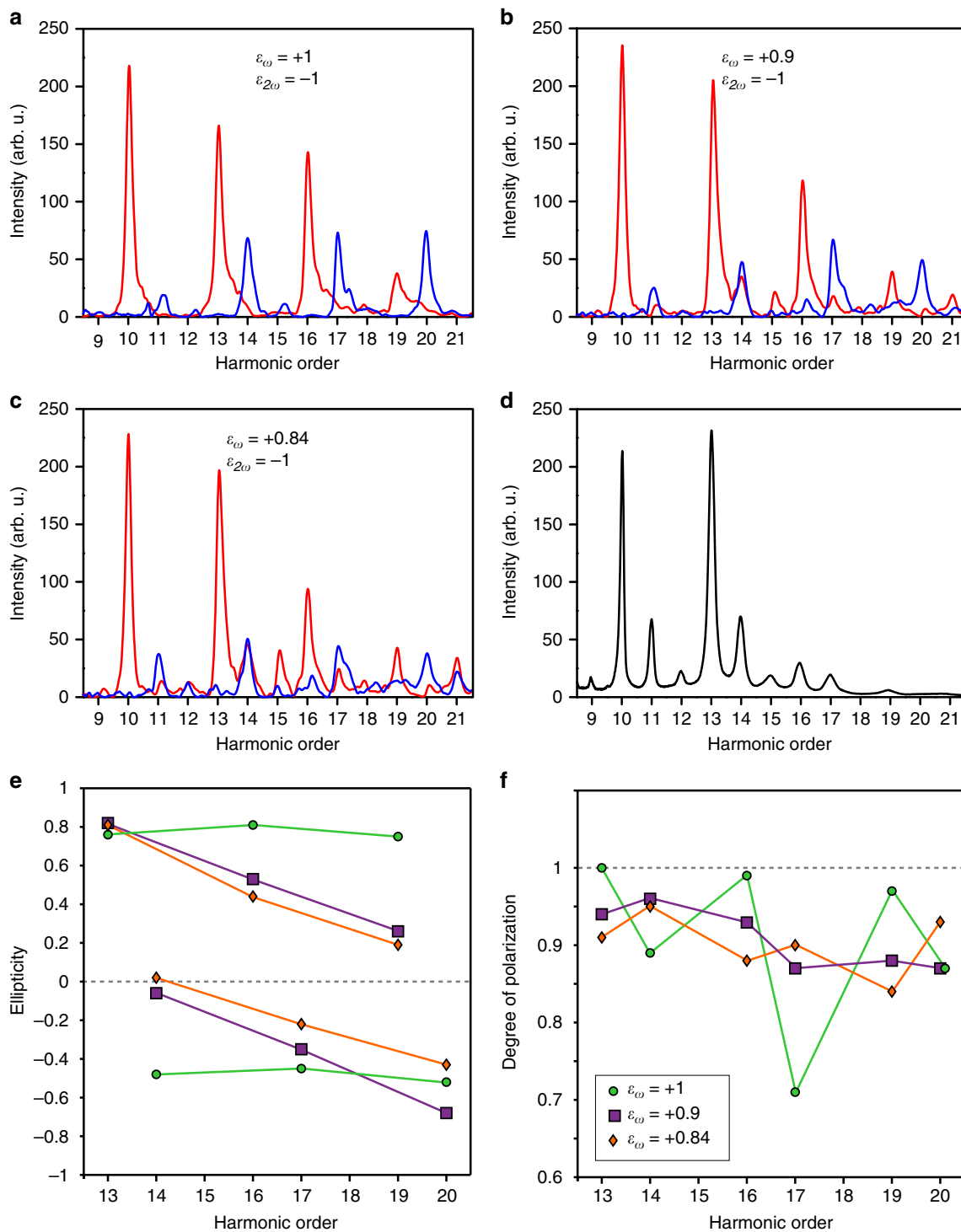


Fig. 3 Effects of a slight ellipticity of the ω driving field in argon. **a–c** High harmonic spectra calculated in argon for trapezoidal pulses of maximal intensity 1.2×10^{14} W/cm² and ω driver ellipticities $\epsilon_{\omega} = +1$ (**a**) + 0.9 (**b**) and + 0.84 (**c**), the 2ω driver being kept perfectly circular ($\epsilon_{2\omega} = -1$). The components co-rotating and counter-rotating with the ω field are shown in red and blue, respectively. **d** Experimental harmonic spectrum generated in argon in the conditions described in Fig. 4 and measured with the XUV spectrometer. **e–f** Ellipticity (**e**) and degree of polarization (**f**) calculated over the harmonic spectral width (+/–0.25 order around the peak), for the $3q+1$ and $3q+2$ orders simulated in the plateau region above the ionization potential of argon

for most orders (Fig. 3e)²⁴. This has been proposed as a simple method to control the harmonic ellipticity for applications¹⁷. However, the simulations reveal that, in the studied conditions, the decreased ellipticity goes together with an increased and more homogeneous depolarization (up to 10–15%) (Fig. 3f).

The non-circularity of one driving field may have further consequences if the ω – 2ω relative phase is not controlled in the

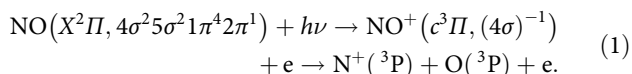
experiments. Indeed, for significant acquisition times, the polarization characteristics (more precisely, the Stokes parameters) will be a weighted average over all possible relative ω – 2ω phases. In a perfectly circular case, a change in relative phase simply rotates in space the threefold rosette shape of the combined driving fields (see Fig. 1b), which has no influence on the –circular– harmonic polarization⁵⁵. In contrast, with one

elliptical driver, in presence of fast ionization or short pulses, this causes a change of the effective electric field over time, and thus of the harmonic polarization characteristics. The simulation of a measurement averaging over twelve different ω - 2ω relative phases in the ($\varepsilon_\omega = +0.9$, $\varepsilon_{2\omega} = -1$) case shows a decreased degree of polarization of H17 to only 61% (Supplementary Note 5). Note finally that macroscopic effects can further affect the polarization of the harmonics^{18,56}, although they can be minimized by using a thin generating medium such as an effusive jet³¹.

Complete measurement of the harmonic polarization state.

The molecular polarimetry method⁴¹, recently extended to probe the complete polarization state of a comb of elliptical high-order harmonics⁴², is here applied to the harmonic emission driven in argon by counter-rotating bichromatic fields. This method is based on the anisotropic interaction between an XUV light field and a molecule resulting in photoionization. It consists in measuring MFPAD, a complete angular observable whose expression encapsulates the s_1 , s_2 , s_3 normalized Stokes parameters of the ionizing light^{57,58}. In particular, the s_3 parameter, scaling the intrinsic light helicity, is derived from the molecular frame circular dichroism in the angular distribution (CDAD), the handedness of the system arising from the non-coplanarity of the molecular axis, the photoelectron momentum and the light propagation axis \mathbf{k} ⁵⁹.

The experiments were conducted on the PLFA beamline (CEA Saclay)⁶⁰ where the XUV pulses generated by the bichromatic field were focused in a COLTRIMS-type reaction microscope⁶¹ to induce photoionization of randomly oriented NO target molecules (Fig. 4 and Methods section). In order to access MFPADs, we take advantage of prompt dissociative photoionization (DPI) selecting the well characterized prototype reaction⁵⁸:



The ($\mathbf{V}_{\text{N}^+}, \mathbf{V}_e$) vector correlation measured for each (N^+, e) coincident event leads to the electron-ion kinetic energy

correlation diagram. The latter enables us to measure the $I(\theta_e, \phi_e, \chi, \gamma)$ MFPAD corresponding to process (1) for each harmonic peak⁴², where (θ_e, ϕ_e) represents the electron emission direction in the MF and (χ, γ) defines the orientation of the molecule in the field frame.

We first illustrate in the first row of Fig. 5 the determination of the s_3 key parameter for harmonics H16 and H17 generated with left circularly-polarized (LCP, $s_{3,\omega} \approx \varepsilon_\omega \approx -1$) ω field and right circularly-polarized (RCP, $s_{3,2\omega} \approx \varepsilon_{2\omega} \approx +1$) 2ω field (for H19, see Supplementary Note 2). Figure 5d, g present the two $I_{\chi=90^\circ}(\theta_e, \phi_e)$ MFPADs for NO molecules oriented perpendicular to the \mathbf{k} vector (averaged on the γ angle)—a geometry emblematic of the CDAD effect. The remarkable right-left asymmetries observed in the MFPADs, maximum in the polarization plane ($\phi_e = 90^\circ$ and 270°), demonstrate the circular character of each harmonic, with helicities of opposite sign for H16 and H17.

These asymmetries are scaled by the $s_3 F_{11}(\theta_e)$ entangled product⁴¹, where $F_{11}(\theta_e)$ is the photoionization dynamical parameter which governs the CDAD for reaction (1) at each photon energy. The extraction of s_3 for each harmonic peak requires calibrated references $F_{11}^R(\theta_e)$. These were recorded using well-defined polarization states at the DESIRS beamline of SOLEIL synchrotron⁶²: $F_{11}^R(\theta_e)$ is positive for such energies, and varies smoothly along the shape resonance of the $\text{NO}^+(c^3\Pi)$ state⁵⁸. For each harmonic, the s_3 parameter is the affinity coefficient which leads to the best fit between the measured $s_3 F_{11}(\theta_e)$ and reference $F_{11}^R(\theta_e)$ functions. The derived s_3 parameters amount to -0.8 for H16 and $+0.53$ for H17 (see Table 1). These values confirm that the helicities of H16 ($3q+1$) and H17 ($3q+2$) possess the sign of the ω and 2ω helicities, respectively, consistent with XMCD measurements^{18,32}. They also evidence their different magnitude, significantly smaller for H17 than for H16¹⁸. We finally demonstrate in the second row of Fig. 5 that the MFPAD right-left asymmetries and subsequent signs of s_3 are reversed when opposite helicities are used for the ω and 2ω fields¹⁸.

The s_1 and s_2 Stokes parameters are extracted from the $I(\chi, \gamma)$ reduced MFPAD after integration over the electron coordinates, that is, the N^+ ion fragment angular distributions in the field

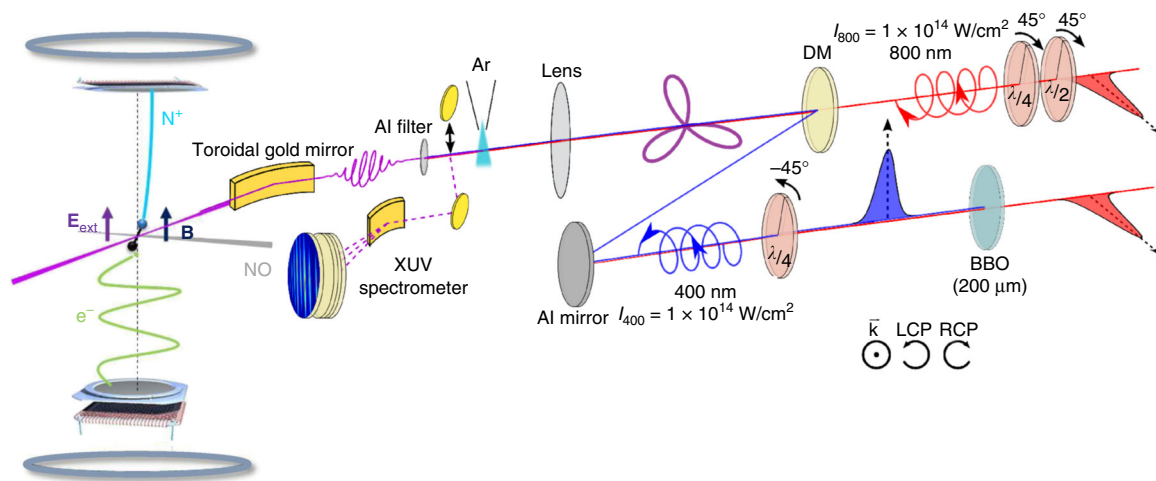


Fig. 4 Experimental setup for the complete characterization of the harmonic polarization state. A 1-kHz 3-mJ 800-nm beam is split into two in a Mach-Zehnder interferometer. In one arm, a BBO crystal generates the 400-nm pulses. A zero-order quarter-wave plate ($\lambda/4$) is placed in each arm to control the ellipticity of the fields, and an additional half-wave plate ($\lambda/2$) is placed in the fundamental arm to rotate its polarization along the s axis. After recombination on a dichroic mirror (DM), the two beams are focused into an argon gas jet for HHG. The XUV emission can be sent to a photon spectrometer with a movable mirror, or filtered with an aluminum foil and refocused by a toroidal mirror at the center of an electron-ion coincidence 3D momentum spectrometer^{42, 60} (and references therein) where it intersects the NO supersonic molecular jet. Electron and ion trajectories are controlled by coupled electric and magnetic fields set in the spectrometer combined with two delay-line time- and position-sensitive detectors, ensuring a 4π collection of both particles for the studied DPI reaction (1). For details see the Methods section

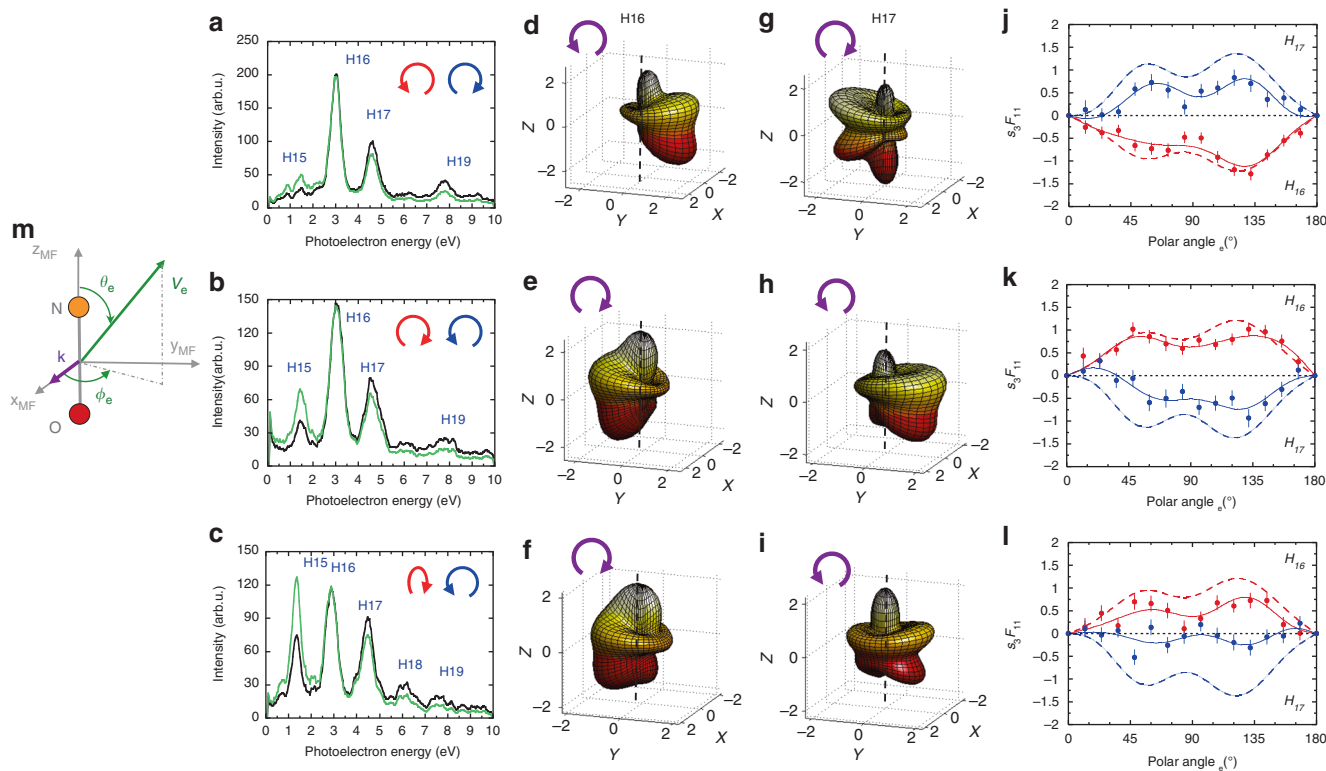


Fig. 5 Harmonic helicities characterized by molecular frame photoemission. The three rows correspond to the counter-rotating ω - 2ω driving fields, as labeled in (a, b, c), first row: LCP ($\epsilon_{\omega} \approx -1$) and RCP ($\epsilon_{2\omega} \approx +1$), second row: RCP ($\epsilon_{\omega} \approx +1$) and LCP ($\epsilon_{2\omega} \approx -1$), third row: right-elliptically polarized ($\epsilon_{\omega} \approx +0.84$) and LCP ($\epsilon_{2\omega} \approx -1$). **a-c** Photoelectron spectra for reaction (1) induced by the harmonic beam, extracted from the electron-ion kinetic energy correlation diagram as described in ref. 42: raw data (black), corrected data accounting for the cross section of reaction (1)⁷³ (green). These spectra are discussed in Supplementary Note 7. **d-f** H16 and **g-i** H17 induced $I_{\chi=90^\circ}(\theta_e, \phi_e)$ MFPADs for reaction (1) with NO oriented perpendicular to the **k** vector as shown in (m). **j-l** $s_3F_{11}(\theta_e)$ (dots and Legendre polynomial line fit) compared to the reference $F_{11}^R(\theta_e)$ functions (dotted line) for photon energies equal to H16 (red) and H17 (blue). $F_{11}^R(\theta_e)$ is displayed with the + or - sign to facilitate comparison with $s_3F_{11}(\theta_e)$. All $F_{11}(\theta_e)$ functions are normalized relative to the isotropic Legendre component of the MFPAD (see Supplementary Note 1). The error bars correspond to twice the standard deviation resulting from a least squares fit in χ , ϕ_e , and γ of the experimental data by the model function (Supplementary Eq. (1))

Table 1 Complete experimental characterization of the harmonic polarization state

800/400	LCP/RCP $\epsilon_{\omega} \approx -1, \epsilon_{2\omega} \approx +1$		RCP/LCP $\epsilon_{\omega} \approx +1, \epsilon_{2\omega} \approx -1$		REP/LCP $\epsilon_{\omega} \approx +0.84, \epsilon_{2\omega} \approx -1$		
Harmonic	H16	H17	H16	H17	H15	H16	H17
s_1	0.27 (0.04)	0.32 (0.05)	0.24 (0.04)	0.07 (0.07)	0.13 (0.07)	0.26 (0.05)	-0.24 (0.08)
s_2	0.05 (0.04)	0.03 (0.05)	-0.12 (0.04)	-0.20 (0.07)	-0.13 (0.07)	-0.34 (0.05)	-0.46 (0.07)
s_3	-0.80 (0.04)	0.53 (0.04)	0.77 (0.04)	-0.53 (0.04)	0.33 (0.07)	0.48 (0.04)	-0.22 (0.05)
s_4	0.15 (0.03)	0.38 (0.04)	0.19 (0.04)	0.43 (0.05)	0.62 (0.07)	0.36 (0.04)	0.43 (0.08)
P	0.85 (0.03)	0.62 (0.04)	0.81 (0.04)	0.57 (0.05)	0.38 (0.07)	0.64 (0.04)	0.57 (0.08)
Ψ ($^\circ$)	5 (4.5)	2.5 (4.5)	167 (5)	144.5 (9.5)	157.5 (13)	154 (4)	121.5 (4)
ϵ	-0.72 (0.04)	0.56 (0.05)	0.71 (0.04)	-0.68 (0.08)	0.58 (0.12)	0.45 (0.05)	-0.21 (0.04)

Normalized Stokes parameters (s_1, s_2, s_3), depolarization factor s_4 , degree of polarization P , ellipse orientation ψ and ellipticity ϵ for H16 and H17 harmonic peaks for the two configurations of the driving fields: LCP/RCP $\approx -1/+1$; RCP/LCP $\approx +1/-1$; and for H15, H16, and H17 for RCP/LCP $\approx 0.84/-1$. Standard deviations are indicated in brackets

frame⁴¹ (see Methods and Supplementary Note 1). They evidence here a rather weak degree of linear polarization of the order of 0.2–0.3 (Table 1). Most importantly, measuring coherently the s_1, s_2, s_3 Stokes vector enables us to determine the degree of polarized light $P = \sqrt{s_1^2 + s_2^2 + s_3^2}$, in addition to the geometric parameters of the polarization ellipse, its orientation angle $\psi = \frac{1}{2} \text{atan}\left(\frac{s_2}{s_1}\right)$ and signed ellipticity $\epsilon = \tan\left(\frac{1}{2} \text{asin}\left(\frac{s_3}{\sqrt{s_1^2 + s_2^2 + s_3^2}}\right)\right)$. Their values are summarized in Table 1, where we also feature the degree of

depolarization $s_4 = 1 - P$. P is found to be significantly smaller than 1, with values smaller for H17 ($P \approx 0.6$) than for H16 ($P \approx 0.83$). The results for the LCP/RCP and RCP/LCP configurations are remarkably consistent and evidence depolarization in the harmonic emission. The ellipticity values are smaller for H17 than for H16, with $|\epsilon| \approx 0.6$ and 0.7 , respectively. We do not comment on the orientation of the ellipse in a context where the time delay ω - 2ω was not stabilized. The results obtained with bicircular counter-rotating fields thus show deviations from circularity for the H16 and H17 harmonic peaks, their polarization state being

described by a large ellipticity (0.6–0.7), a weak degree of linear polarization (0.2–0.3) comparable for both, and an unpolarized component larger for H17 (0.4 versus 0.2).

Finally, the third row in Fig. 5 and the right columns in Table 1 display the results when the ω field ellipticity is reduced to $\varepsilon_\omega \approx +0.84$ (rotation of 5° of the quarter-wave plate) with the 2ω field kept quasi-circular ($\varepsilon_{2\omega} \approx -1$): the harmonic ellipticity is strongly reduced¹⁷, H16 keeping a higher helicity than H17. The photoelectron spectrum shows a significant increase of H15 ($3q$) intensity, allowing the measurement of an ellipticity of same sign as that of H16, and a high depolarization (Supplementary Note 2). Beyond the statistical uncertainties characterized by the standard deviation (Table 1), a higher accuracy in the polarization state description will benefit from an improved instrumental context (advanced calibration of the optical elements, perfect control of the driving fields CEP and relative phase, ...). A major increase of the repetition rate of the driving laser, up to 10 or 100 kHz, will be highly beneficial, since the reported coincidence study at 1 kHz imposed a 2–3 h duration for each measurement.

Discussion

The reported results provide the complete in situ determination of the polarization state of high harmonics generated by bicircular counter-rotating fields. In particular, the degree of polarization, long assumed to be unity, is here measured. Together with TDSE calculations, the experiments indicate that this scheme may generate non-circular harmonics with polarization characteristics varying spectrally, thus responsible for depolarization. In light of the numerical study, the deviation from circularity and depolarization measured in our experimental conditions partially originate from the fast ionization of the argon generating gas, together with the slight elliptical character of the ω driver. These deleterious effects are enhanced by the averaging over multiple ω – 2ω relative phases in the interferometer. Furthermore, short-pulse envelope effects, probably limited in our experiments, may play a significant role at shorter pulse durations as evidenced by simulations.

This study helps defining optimal generation conditions for ultrashort circularly-polarized high harmonics. Short-pulse envelope effects will be minimized by using shaped top-hat, CEP-stable driving laser pulses. The relative time delay between the two pulses should be actively controlled⁶³, or passively stabilized by a compact in-line interferometer⁶⁴. Finally, ionization of the generation medium should be avoided, which points toward light rare gases driven by mid-IR driving lasers^{32,38}, ensuring a broad harmonic spectrum while keeping low ionization rates. The complete characterization and further optimization of circular harmonic emission will allow advanced studies of chiral-sensitive light–matter interactions such as ultrafast chiral recognition via photoelectron circular dichroism^{65–67}, ultrafast magnetization and spin dynamics^{5,68,69}.

Methods

Experimental setup. Experiments have been performed at the PLFA facility (CEA-Saclay, SLIC) based on a Ti:Sapphire laser delivering 800 nm, 50 fs pulses with 13 mJ energy at 1 kHz repetition rate⁶⁰. The 800 nm beam is separated by a 50/50 beam-splitter at the entrance of a Mach–Zehnder interferometer. In one arm, a BBO crystal (200- μ m thick, 31° cut angle) generates the 400 nm, 250 μ J second harmonic pulses. A zero-order quarter-wave plate is placed in each arm to control the ellipticity of the fields, and an additional half-wave plate is placed in the fundamental arm to rotate its polarization along the s axis during optimization phases. After recombination on a dichroic mirror, both beams are focused with a lens ($f = 80$ cm) into an argon gas jet to generate an APT mainly composed of $3q + 1$ and $3q + 2$ high-order harmonics (HH). The intensity of the two beams is determined with the cutoff law of the XUV spectrum, when the high harmonics are generated with a single color, linearly polarized. We estimate an equal intensity at focus, $I_\omega \approx I_{2\omega} \approx 1 \times 10^{14}$ W/cm². The relative delay between the two arms is set by a

translation stage. Their temporal overlap is determined by maximizing the generation of the harmonics orders produced only when both ω and 2ω fields are present (that is, even harmonics of the 2ω field, here H8, H12, and H16), with linearly-polarized pulses.

With a movable gold mirror, the XUV emission can be sent to a spectrometer composed of a XUV grating, two micro channel plates and a phosphor screen detector and a CCD camera. After optimization and filtering by an aluminum foil (200 nm), the XUV radiation is focused by a gold-coated toroidal mirror (angle of incidence 78.5° , $f = 60$ cm) at the center of the ion–electron coincidence 3D momentum spectrometer CIEL as described in ref. ⁴². Note that the reflection on this mirror modifies the polarization state of the incoming HHs, see Supplementary Note 3. The intersection of the XUV light with the NO molecular beam produced in a supersonic expansion defines the interaction region where photoionization occurs. Ions and electrons are extracted and guided to their respective time- and position-sensitive delay-line detector (TPSD, RoentDek) by coupled electric and magnetic fields, which ensure a 4π collection of both particles for the studied dissociative photoionization (DPI) processes (Eq. (1))^{42,60} and references therein. The ensemble allows for measuring in coincidence the initial 3D velocity vectors of the ion fragment V_{N^+} and the photoelectron V_e resulting from the same DPI event. At the 1 kHz repetition rate of the Ti:Sapphire laser, which restricts the total number of coincidences to about 50 c/s, each measurement lasted for a few hours requiring a good stability of the setup.

Determination of the Stokes parameters for each harmonic. The (s_1, s_2, s_3) normalized Stokes parameters for each HH were determined using the molecular polarimetry method (MP) demonstrated in ref. ⁴¹. Taking advantage of dissociative photoionization (DPI) of small molecules characterized by electron-ion coincident 3D momentum spectrometry, MP consists in measuring the $I(\theta_e, \phi_e, \chi, \gamma)$ MFPAD for selected DPI processes, where (χ, γ) define the polar and azimuthal recoil-ion emission direction in the laboratory frame (LF), and (θ_e, ϕ_e) the polar and azimuthal photoelectron emission direction in the molecular frame (MF). $I(\theta_e, \phi_e, \chi, \gamma)$ encodes the (s_1, s_2, s_3) Stokes parameters⁵⁸ of the ionizing light. DPI of the NO molecule into the $\text{NO}^+(c^3\Pi)$ ionic state (see Eq. (1)) is here induced by each peak of the studied harmonic comb⁴². Exploiting the general form of the MFPAD (see Supplementary Eq. (1)) leads to the product $s_3 \times F_{11}(\theta_e)$ and therefore to the s_3 Stokes parameter, if the $F_{11}(\theta_e)$ reference functions characterizing the MF circular dichroism for reaction Eq. (1) at the HH photon energy are determined. The s_1 and s_2 Stokes parameters are derived from the $I(\chi, \gamma)$ LF ion fragment angular distribution after integrating the $I(\theta_e, \phi_e, \chi, \gamma)$ MFPAD over the electron emission angles. For details see the Supplementary Note 1.

Theoretical methods. We solve numerically the TDSE in the velocity gauge, on a two-dimensional (2D) Cartesian grid. We first compute the eigenvalues and eigenstates of the stationary Hamiltonian, by means of the imaginary time propagation method, for a soft-core screened Coulomb atomic potential reproducing the ionization potential I_p of the considered atom (argon $I_p = 0.579$ a.u. or helium $I_p = 0.903$ a.u., where a.u. stands for atomic units), and the $3p_x$ and $3p_y$ orbitals for argon:

$$V(x, y) = -\frac{(Z-1)e^{-(x^2+y^2)} + 1}{\sqrt{x^2 + y^2 + \eta}}$$

with $Z = 18$ and $\eta = 1.04327$ for argon, and $Z = 2$, $\eta = 0.67724$ for helium. The $3p$ ($m = \pm 1$) states of argon are constructed from the $3p_x$ and $3p_y$ orbitals: $3p(m = \pm 1) = 3p_x \pm i3p_y$. The high laser intensity can mix the degenerate p orbitals⁷⁰, so that we do not discuss the relative influence of the co-rotating and counter-rotating orbitals here²⁸. The initial wave functions are then propagated forward in time using the split step Fourier method⁷¹. To avoid spurious effects when the wave packet reaches the boundary of the computational domain, we apply the wavelength-dependent absorption method⁷² at each time step.

The grid size is 819.2×819.2 a.u. and the spatial step size is $\Delta x = \Delta y = 0.2$ a.u. The depth of the absorbing layer is 8 a.u. on each side of the grid, along both x - and y -axis. Note that the grid size was chosen much larger than the maximum wave packet quivering amplitude (~ 20 – 30 a.u. in the case of He), and could accommodate for strong ionization without significant loss of wavefunction amplitude. We systematically checked the time evolution of the norm of the wavefunction all along the simulations. The time step is $\Delta t = 6.2 \times 10^{-2}$ a.u. The accuracy is $O(\Delta t)^3$. The (relative) spatial frequency resolution is $\frac{\Delta k_x}{k_0} = \frac{\Delta k_y}{k_0} = \frac{\lambda_0}{\Delta x} = \frac{\lambda_0}{\Delta y} = 7.5 \times 10^4$, and the (relative) temporal frequency resolution is $\frac{\Delta \omega}{\omega_0} = \frac{T}{\Delta t} = 1.6 \times 10^3$. This ensures a very accurate description of the relatively low-order harmonics considered in this work.

The laser field is the sum of two counter-rotating circularly polarized waves at $\lambda_1 = 800$ nm and $\lambda_2 = 400$ nm central wavelengths, respectively:

$$\mathbf{E}(t) = f(t) \left\{ \begin{array}{l} [E_1 \cos(\omega_1 t + \varphi_{\text{IR}} + \varphi_{\text{CEP}}) + E_2 \cos(\omega_2 t + 2\varphi_{\text{CEP}})] \mathbf{e}_x \\ + [E_1 \varepsilon_1 \sin(\omega_1 t + \varphi_{\text{IR}} + \varphi_{\text{CEP}}) + E_2 \varepsilon_2 \sin(\omega_2 t + 2\varphi_{\text{CEP}})] \mathbf{e}_y \end{array} \right\}$$

with $\omega_2 = 2 \times \omega_1$, $E_i = \frac{E_0}{\sqrt{1+\varepsilon_i^2}}$, and ε_i the field ellipticity, $i = 1, 2$. φ_{CEP} is the carrier-

envelope phase, acting on both ω_1 and ω_2 fields, whereas φ_{IR} is a phenomenological phase term applied only on the IR field for simulating a dephasing between the two fields induced, e.g., by instabilities in the Mach-Zehnder interferometer used to split the beams (see Fig. 4). The pulse envelope $f(t)$ has a sine square shape with five- ω -cycle FWHM in Fig. 1, and a trapezoidal shape with a two-IR cycle turn-on, a six-cycle plateau, and a two-cycle turn-off in Fig. 2, 3. In all the presented figures, $\varphi_{\text{CEP}} = 0$.

High-order harmonic spectra are obtained by Fourier-transforming the time-dependent, space-integrated components of the dipole acceleration. For characterizing the polarization properties of the harmonics, we calculate the Stokes parameters³⁴ following the method described in ref. 13. The Stokes parameters are further averaged over a spectral width $\Delta\omega$ around the harmonic central frequency Ω according to: $S_i(\Omega) = \int_{\Omega-\frac{\Delta\omega}{2}}^{\Omega+\frac{\Delta\omega}{2}} S_i(\omega) d\omega$, and the normalized Stokes parameters are calculated following $s_i(\Omega) = \frac{S_i(\Omega)}{S_0(\Omega)}$.

We emphasize here that the HHG process being coherent, the emission is fully polarized for each frequency inside the harmonic peak. However, the polarization characteristics may vary spectrally for reasons discussed above. Consequently, the spectrally-integrated emission of a particular harmonic (corresponding to the emission during the whole harmonic temporal profile) may exhibit a reduced degree of polarization.

Code availability. The custom computer code used in the current study is available from the corresponding authors on reasonable request.

Data availability

The datasets generated during the current study are available from the corresponding authors on reasonable request.

Received: 13 April 2018 Accepted: 17 October 2018

Published online: 09 November 2018

References

- Barron, L. *Molecular Light Scattering and Optical Activity* (Cambridge University Press, 2004).
- Stöhr, J. Exploring the microscopic origin of magnetic anisotropies with X-ray magnetic circular dichroism (XMCD) spectroscopy. *J. Magn. Magn. Mater.* **200**, 470–497 (1999).
- Thole, B. T., Carra, P., Sette, F. & van der Laan, G. X-ray circular dichroism as a probe of orbital magnetization. *Phys. Rev. Lett.* **68**, 1943–1946 (1992).
- Ferré, A. et al. A table-top ultrashort light source in the extreme ultraviolet for circular dichroism experiments. *Nat. Photonics* **9**, 93–98 (2015).
- Boeglin, C. et al. Distinguishing the ultrafast dynamics of spin and orbital moments in solids. *Nature* **465**, 458–461 (2010).
- Radu, I. et al. Transient ferromagnetic-like state mediating ultrafast reversal of antiferromagnetically coupled spins. *Nature* **472**, 205–208 (2011).
- Rouxel, J. R., Kowalewski, M. & Mukamel, S. Photoinduced molecular chirality probed by ultrafast resonant X-ray spectroscopy. *Struct. Dyn.* **4**, 044006 (2017).
- Allaria, E. et al. Control of the polarization of a vacuum-ultraviolet, high-gain, free-electron laser. *Phys. Rev. X* **4**, 041040 (2014).
- Lutman, A. et al. Polarization control in an X-ray free-electron laser. *Nat. Photonics* **10**, 468–472 (2016).
- Corkum, P. B. Plasma perspective on strong field multiphoton ionization. *Phys. Rev. Lett.* **71**, 1994–1997 (1993).
- Budil, K., Salières, P., L’Huillier, A., Ditmire, T. & Perry, M. Influence of ellipticity on harmonic generation. *Phys. Rev. A* **48**, R3437 (1993).
- Weihe, F. & Bucksbaum, P. Measurement of the polarization state of high harmonics generated in gases. *JOSA B* **13**, 157–161 (1996).
- Antoine, P., Carré, B., L’Huillier, A. & Lewenstein, M. Polarization of high-order harmonics. *Phys. Rev. A* **55**, 1314–1324 (1997).
- Zhou, X. et al. Elliptically polarized high-order harmonic emission from molecules in linearly polarized laser fields. *Phys. Rev. Lett.* **102**, 073902 (2009).
- Mairesse, Y. et al. High harmonic spectroscopy of multichannel dynamics in strong-field ionization. *Phys. Rev. Lett.* **104**, 213601 (2010).
- Vodungbo, B. et al. Polarization control of high order harmonics in the euv photon energy range. *Opt. Express* **19**, 4346–4356 (2011).
- Fleischer, A., Kfir, O., Diskin, T., Sidorenko, P. & Cohen, O. Spin angular momentum and tunable polarization in high-harmonic generation. *Nat. Photonics* **8**, 543–549 (2014).
- Kfir, O. et al. Generation of bright phase-matched circularly-polarized extreme ultraviolet high harmonics. *Nat. Photonics* **9**, 99–105 (2015).
- Lambert, G. et al. Towards enabling femtosecond helicity-dependent spectroscopy with high-harmonic sources. *Nat. Commun.* **6**, 6167 (2015).
- Hickstein, D. D. et al. Non-collinear generation of angularly isolated circularly polarized high harmonics. *Nat. Photonics* **9**, 743–750 (2015).
- Skantzakis, E. et al. Polarization shaping of high-order harmonics in laser-aligned molecules. *Sci. Rep.* **6**, 39295 (2016).
- Eichmann, H. et al. Polarization-dependent high-order two-color mixing. *Phys. Rev. A* **51**, R3414–R3417 (1995).
- Long, S., Becker, W. & McIver, J. K. Model calculations of polarization-dependent two-color high-harmonic generation. *Phys. Rev. A* **52**, 2262–2278 (1995).
- Milošević, D. B., Becker, W. & Kopold, R. Generation of circularly polarized high-order harmonics by two-color coplanar field mixing. *Phys. Rev. A* **61**, 063403 (2000).
- Yuan, K.-J. & Bandrauk, A. D. Circularly polarized attosecond pulses from molecular high-order harmonic generation by ultrashort intense bichromatic circularly and linearly polarized laser pulses. *J. Phys. B: At., Mol. Opt. Phys.* **45**, 074001 (2012).
- Pisanty, E., Sukiasyan, S. & Ivanov, M. Spin conservation in high-order-harmonic generation using bicircular fields. *Phys. Rev. A* **90**, 043829 (2014).
- Milošević, D. B. High-order harmonic generation by a bichromatic elliptically polarized field: conservation of angular momentum. *J. Phys. B: At. Mol. Opt. Phys.* **48**, 171001 (2015).
- Medišauskas, L., Wragg, J., Hart, H. & Ivanov, M. Generating isolated elliptically polarized attosecond pulses using bichromatic counterrotating circularly polarized laser fields. *Phys. Rev. Lett.* **115**, 153001 (2015).
- Bandrauk, A. D., Mauger, F. & Yuan, K.-J. Circularly polarized harmonic generation by intense bicircular laser pulses: electron recollision dynamics and frequency dependent helicity. *J. Phys. B: At., Mol. Opt. Phys.* **49**, 23LT01 (2016).
- Jiménez-Galán, A. et al. Control of attosecond light polarization in two-color bicircular fields. *Phys. Rev. A* **97**, 023409 (2018).
- Baykuseva, D., Ahsan, M., Lin, N. & Wörner, H. Bicircular high-harmonic spectroscopy reveals dynamical symmetries of atoms and molecules. *Phys. Rev. Lett.* **116**, 123001 (2016).
- Fan, T. et al. Bright circularly polarized soft X-ray high harmonics for X-ray magnetic circular dichroism. *PNAS* **112**, 14206–14211 (2015).
- Neufeld, O., Podolsky, D., & Cohen, O. Symmetries and selection rules in high harmonic generation and other floquet systems. Preprint at <http://arxiv.org/abs/1706.01087> (2017).
- Born, M. & Wolf, E. *Principles of Optics* 6th edn (Cambridge University Press, 1980).
- Ruf, H. et al. Inhomogeneous high harmonic generation in krypton clusters. *Phys. Rev. Lett.* **110**, 083902 (2013).
- Zhavoronkov, N. & Ivanov, M. Extended ellipticity control for attosecond pulses by high harmonic generation. *Opt. Lett.* **42**, 4720–4723 (2017).
- Milošević, D. B. Circularly polarized high harmonics generated by a bicircular field from inert atomic gases in the p state: a tool for exploring chirality-sensitive processes. *Phys. Rev. A* **92**, 043827 (2015).
- Baykuseva, D., Brennecke, S., Lein, M. & Wörner, H. J. Signatures of electronic structure in bicircular high-harmonic spectroscopy. *Phys. Rev. Lett.* **119**, 203201 (2017).
- Dorney, K. M. et al. Helicity-selective enhancement and polarization control of attosecond high harmonic waveforms driven by bichromatic circularly polarized laser fields. *Phys. Rev. Lett.* **119**, 063201 (2017).
- Zuo, T. & Bandrauk, A. D. High-order harmonic generation in intense laser and magnetic fields. *J. Nonlinear Opt. Phys. & Mater.* **4**, 533–546 (1995).
- Veyrinas, K. et al. Complete determination of the state of elliptically polarized light by electron-ion vector correlations. *Phys. Rev. A* **88**, 063411 (2013).
- Veyrinas, K. et al. Molecular frame photoemission by a comb of elliptical high-order harmonics: a sensitive probe of both photodynamics and harmonic complete polarization state. *Faraday Discuss.* **194**, 161–183 (2016).
- Milošević, D. B. & Becker, W. Attosecond pulse trains with unusual nonlinear polarization. *Phys. Rev. A* **62**, 011403 (2000).
- Jiménez-Galán, A., Zhavoronkov, N., Schloz, M., Morales, F. & Ivanov, M. Time-resolved high harmonic spectroscopy of dynamical symmetry breaking in bi-circular laser fields: the role of Rydberg states. *Opt. Expr.* **25**, 22880–22896 (2017).
- Yuan, K.-J. & Bandrauk, A. D. Symmetry in circularly polarized molecular high-order harmonic generation with intense bicircular laser pulses. *Phys. Rev. A* **97**, 023408 (2018).
- Lewenstein, M., Salières, P. & L’Huillier, A. Phase of the atomic polarization in high-order harmonic generation. *Phys. Rev. A* **52**, 4747–4754 (1995).
- Bellini, M. et al. Temporal coherence of ultrashort high-order harmonic pulses. *Phys. Rev. Lett.* **81**, 297–300 (1998).
- Chang, Z. et al. Temporal phase control of soft-x-ray harmonic emission. *Phys. Rev. A* **58**, R30–R33 (1998).
- Salières, P. et al. Feynman’s path-integral approach for intense-laser-atom interactions. *Science* **292**, 902–905 (2001).

50. Salières, P., L'Huillier, A. & Lewenstein, M. Coherence control of high-order harmonics. *Phys. Rev. Lett.* **74**, 3776–3779 (1995).
51. Watson, J. B., Sanpera, A. & Burnett, K. Pulse-shape effects and blueshifting in the single-atom harmonic generation from neutral species and ions. *Phys. Rev. A* **51**, 1458–1463 (1995).
52. Kan, C., Capjack, C. E., Rankin, R. & Burnett, N. H. Spectral and temporal structure in high harmonic emission from ionizing atomic gases. *Phys. Rev. A* **52**, R4336–R4339 (1995).
53. Schafer, K. J. & Kulander, K. C. High harmonic generation from ultrafast pump lasers. *Phys. Rev. Lett.* **78**, 638–641 (1997).
54. Salières, P., Antoine, P., de Bohan, A. & Lewenstein, M. Temporal and spectral tailoring of high-order harmonics. *Phys. Rev. Lett.* **81**, 5544–5547 (1998).
55. Kfir, O. et al. Helicity-selective phase-matching and quasi-phase matching of circularly polarized high-order harmonics: towards chiral attosecond pulses. *J. Phys. B: At. Mol. Opt. Phys.* **49**, 123501 (2016).
56. Antoine, P., L' Huillier, A., Lewenstein, M., Salières, P. & Carré, B. Theory of high-order harmonic generation by an elliptically polarized laser field. *Phys. Rev. A* **53**, 1725 (1996).
57. Doweck, D. & Lucchese, R. R. in *Dynamical Processes in Atomic and Molecular Physics*, 57–95 (Bentham Science Publishers, 2012).
58. Lebech, M. et al. Complete description of linear molecule photoionization achieved by vector correlations using the light of a single circular polarization. *J. Chem. Phys.* **118**, 9653–9663 (2003).
59. Dubs, R. L., Dixit, S. N. & McKoy, V. Circular dichroism in photoelectron angular distributions from oriented linear molecules. *Phys. Rev. Lett.* **54**, 1249–1251 (1985).
60. Weber, S. J. et al. Flexible attosecond beamline for high harmonic spectroscopy and XUV/near-IR pump probe experiments requiring long acquisition times. *Rev. Sci. Instrum.* **86**, 033108 (2015).
61. Ullrich, J. et al. Recoil-ion and electron momentum spectroscopy: reaction-microscopes. *Rep. Progress. Phys.* **66**, 1463 (2003).
62. Nahon, L. et al. DESIRS: a state-of-the-art VUV beamline featuring high resolution and variable polarization for spectroscopy and dichroism at SOLEIL. *J. Synchrotron Radiat.* **19**, 508–520 (2012).
63. Chen, C. et al. Tomographic reconstruction of circularly polarized high-harmonic fields: 3D attosecond metrology. *Sci. Adv.* **2**, e1501333 (2016).
64. Kfir, O. et al. In-line production of a bi-circular field for generation of helically polarized high-order harmonics. *Appl. Phys. Lett.* **108**, 211106 (2016).
65. Böwering, N. et al. Asymmetry in photoelectron emission from chiral molecules induced by circularly polarized light. *Phys. Rev. Lett.* **86**, 1187–1190 (2001).
66. Nahon, L., Garcia, G. A. & Powis, I. Valence shell one-photon photoelectron circular dichroism in chiral systems. *J. Electron Spectrosc. Relat. Phenom.* **204**, 322–334 (2015).
67. Beaulieu, S. et al. Attosecond-resolved photoionization of chiral molecules. *Science* **358**, 1288–1294 (2017).
68. Kfir, O. et al. Nanoscale magnetic imaging using circularly polarized high-harmonic radiation. *Sci. Adv.* **3**, ea04641 (2017).
69. Willems, F. et al. Probing ultrafast spin dynamics with high-harmonic magnetic circular dichroism spectroscopy. *Phys. Rev. B* **92**, 220405(R) (2015).
70. Barth, I. & Lein, M. Numerical verification of the theory of nonadiabatic tunnel ionization in strong circularly polarized laser fields. *J. Phys. B: At. Mol. Opt. Phys.* **47**, 204016 (2014).
71. Feit, M., Fleck, J. & Steiger, A. Solution of the Schrodinger equation by a spectral method. *J. Comput. Phys.* **47**, 412–433 (1982).
72. Strelkov, V. V., Khokhlova, M. A., Gonoskov, A. A., Gonoskov, I. A. & Ryabikin, M. Y. High-order harmonic generation by atoms in an elliptically polarized laser field: harmonic polarization properties and laser threshold ellipticity. *Phys. Rev. A* **86**, 013404 (2012).
73. Iida, Y., Carnovale, F., Daviel, S. & Brion, C. E. Absolute oscillator strengths for photoabsorption and the molecular and dissociative photoionization of nitric oxide. *Chem. Phys.* **105**, 211–225 (1986).

Acknowledgements

The authors gratefully acknowledge J. Guigand, S. Lupone, and N. Tournier (ISMO) for their efficient technical support for maintenance of the COLTRIMS set-up. This research was supported by the EU-H2020-MSCA-ITN-MEDEA-641789, EU-H2020-LASERLAB-EUROPE-654148, the ANR-15-CE30-0001-CIMBAAD, ANR-11-EQPX0005-ATTO-LAB, ANR-10-LABX-0039-PALM, and Région Ile-de-France SESAME2012-ATTOLITE.

Author contributions

L.B., K.V. and V.G. contributed equally to this work. K.V., J.-C.H. and D.D. operated the COLTRIMS acquisition, analyzed the molecular polarimetry data and discussed the results with all the authors. V.G., S.J.W., L.B., B.C. and P.S. operated the optical and high-harmonic beamlines in the bichromatic circularly-polarized configuration. J.-F.H. and F.L. operated the PLFA laser. T.A. performed the numerical simulations. T.A., L.B. and P.S. discussed the numerical results with inputs from all the authors. L.B., K.V., V.G., J.-C.H., P.S. and D.D. wrote a first version of the manuscript; all the authors contributed to the final version.

Additional information

Supplementary Information accompanies this paper at <https://doi.org/10.1038/s41467-018-07151-8>.

Competing interests: The authors declare no competing interests.

Reprints and permission information is available online at <http://npg.nature.com/reprintsandpermissions/>

Publisher's note: Springer Nature remains neutral with regard to jurisdictional claims in published maps and institutional affiliations.

 **Open Access** This article is licensed under a Creative Commons Attribution 4.0 International License, which permits use, sharing, adaptation, distribution and reproduction in any medium or format, as long as you give appropriate credit to the original author(s) and the source, provide a link to the Creative Commons license, and indicate if changes were made. The images or other third party material in this article are included in the article's Creative Commons license, unless indicated otherwise in a credit line to the material. If material is not included in the article's Creative Commons license and your intended use is not permitted by statutory regulation or exceeds the permitted use, you will need to obtain permission directly from the copyright holder. To view a copy of this license, visit <http://creativecommons.org/licenses/by/4.0/>.

© The Author(s) 2018